A&A 386, 319–330 (2002)
DOI: 10.1051/0004-6361:20020097

Astronomy & Astrophysics

Discovery of X–rays from Venus with Chandra

K. Dennerl[1], V. Burwitz[1], J. Englhauser[1], C. Lisse[2], and S. Wolk[3]

[1] Max–Planck–Institut für extraterrestrische Physik, Giessenbachstraße, 85748 Garching, Germany
[2] University of Maryland, Department of Astronomy, College Park, MD 20742, USA
[3] Chandra X–Ray Center, Harvard–Smithsonian Center for Astrophysics, 60 Garden Street, Cambridge, MA 02138, USA

Received 28 September 2001 / Accepted 17 January 2002

Abstract. On January 10 and 13, 2001, Venus was observed for the first time with an X–ray astronomy satellite. The observation, performed with the ACIS–I and LETG/ACIS–S instruments on Chandra, yielded data of high spatial, spectral, and temporal resolution. Venus is clearly detected as a half–lit crescent, with considerable brightening on the sunward limb. The morphology agrees well with that expected from fluorescent scattering of solar X–rays in the planetary atmosphere. The radiation is observed at discrete energies, mainly at the O–K$_\alpha$ energy of 0.53 keV. Fluorescent radiation is also detected from C–K$_\alpha$ at 0.28 keV and, marginally, from N–K$_\alpha$ at 0.40 keV. An additional emission line is indicated at 0.29 keV, which might be the signature of the C 1s $\rightarrow \pi^\star$ transition in CO_2 and CO. Evidence for temporal variability of the X–ray flux was found at the 2.6 σ level, with fluctuations by factors of a few times indicated on time scales of minutes. All these findings are fully consistent with fluorescent scattering of solar X–rays. No other source of X–ray emission was detected, in particular none from charge exchange interactions between highly charged heavy solar wind ions and atmospheric neutrals, the dominant process for the X–ray emission of comets. This is in agreement with the sensitivity of the observation.

Key words. atomic processes – molecular processes – scattering – Sun: X–rays, gamma rays – planets and satellites: individual: Venus – X–rays: general

1. Introduction

The first detection of X–ray emission from a planetary atmosphere came as a surprise, when unexpectedly high background radiation was observed in 1967 during a daytime stellar X–ray survey by a rocket (Grader et al. 1968). This radiation was correctly attributed to X–ray fluorescence of the Earth's atmosphere. Aikin (1970) estimated that the same process should also cause other planetary atmospheres to glow in X–rays, although the expected flux at Earth orbit would be extremely small and only detectable with sophisticated instrumentation. X–ray fluorescence of the Earth atmosphere, however, became a well–known component of the X–ray background of satellites in low–Earth orbit. Its properties and its impact on observations were studied in detail by Fink et al. (1988) and Snowden & Freyberg (1993).

The detection of unexpectedly bright X–ray emission from comets (Lisse et al. 1996; Dennerl et al. 1997; Mumma et al. 1997) has led to increased interest in X–ray studies of solar system objects. With its carbon and oxygen rich atmosphere, the absence of a strong magnetic field, and its proximity to the Sun, Venus represents a close planetary analog to a comet. Dissociative recombination of O_2^+ in the Venus ionosphere leads to a hot oxygen exosphere out to over 4000 km (Russell et al. 1985), resembling a cometary coma. To investigate the X–ray properties of Venus, we performed a pioneering observation with the X–ray astronomy satellite Chandra.

Orbiting the Sun at heliocentric distances of 0.718–0.728 astronomical units (AU), the angular separation of Venus from the Sun, as seen from Earth, never exceeds 47.8 degrees. While the observing window of imaging X–ray astronomy satellites is usually restricted to solar elongations of at least 60°, Chandra is the first such satellite which is able to observe as close as 45° from the limb of the Sun. Thus, with Chandra an observation of Venus with an imaging X–ray astronomy satellite became possible for the first time. The observation was scheduled to take place around the time of greatest eastern elongation, when Venus was 47° away from the Sun. At that time it appeared optically as a very bright (−4.4 mag), approximately half–illuminated crescent with a diameter of 23″ (Table 1).

2. Observation and data analysis

Venus is the celestial object with the highest optical surface brightness after the Sun and a highly challenging target for an X–ray observation with Chandra, as the X–ray detectors there (CCDs and microchannel plates) are also

Send offprint requests to: K. Dennerl, e-mail: kod@mpe.mpg.de

Table 1. Journal of observations and observing geometry.

obsid	date 2001	time [UT]	exp time [s]	instrument	r [AU]	Δ [AU]	phase [°]	elong [°]	diam [″]
2411	Jan. 10	19:32:47–21:11:55	5948	LETG/ACIS–S	0.722	0.734	85.0	47.0	22.7
2414	Jan. 10	21:24:30–23:00:26	5756	LETG/ACIS–S	0.722	0.734	85.0	47.0	22.8
583	Jan. 13	12:39:51–15:57:40	11 869	ACIS–I	0.721	0.714	86.5	47.1	23.4

Obsid: Chandra observation identifier, exp time: exposure time, r: distance from Sun, Δ: distance from Earth, phase: angle Sun–Venus–Earth, elong: angle Sun–Earth–Venus, diam: angular diameter.

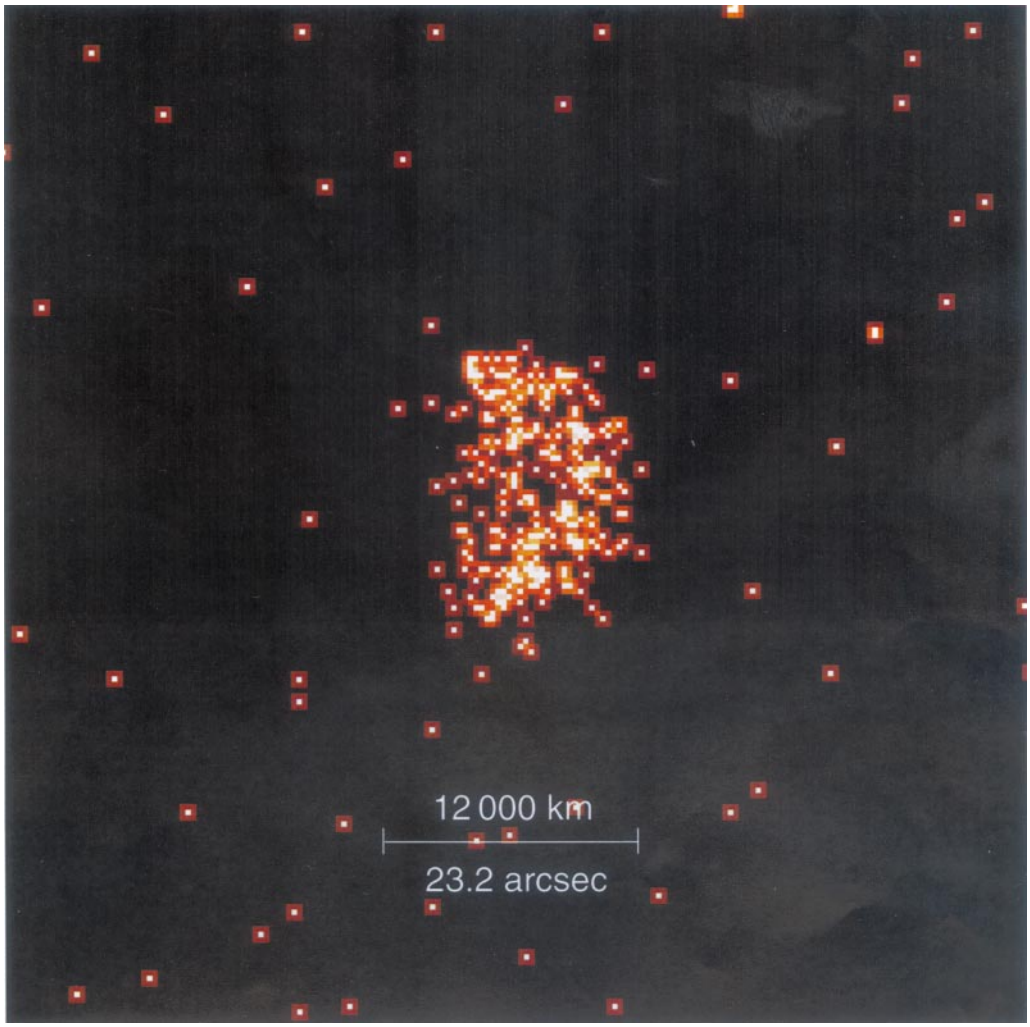

Fig. 1. First X–ray image of Venus, obtained with Chandra ACIS–I on 13 January 2001.

sensitive to optical light. Suppression of optical light is achieved by optical blocking filters which, however, must not attenuate the X–rays significantly. The observation was originally planned to use the back–illuminated ACIS–S3 CCD, which has the highest sensitivity to soft ($E <$ 1.4 keV) X–rays, for direct imaging of Venus, utilizing the intrinsic energy resolution for obtaining spectral information. Before the observation was scheduled, however, it turned out that the optical filter on this CCD would not be sufficient for blocking the extremely high optical flux from Venus. Therefore, half of the observation (obsid 583, cf. Table 1) was performed with the front–illuminated CCDs of the ACIS–I array (I1 and I3), which are less sensitive to soft X–rays, but which are also significantly less affected by optical light contamination.

In order to avoid any ambiguity in the X–ray spectrum due to residual optical light, the other half of the observation (obsid 2411 and 2414, cf. Table 1) was performed with the low energy transmission grating (LETG), where the optical and X–ray spectra are completely

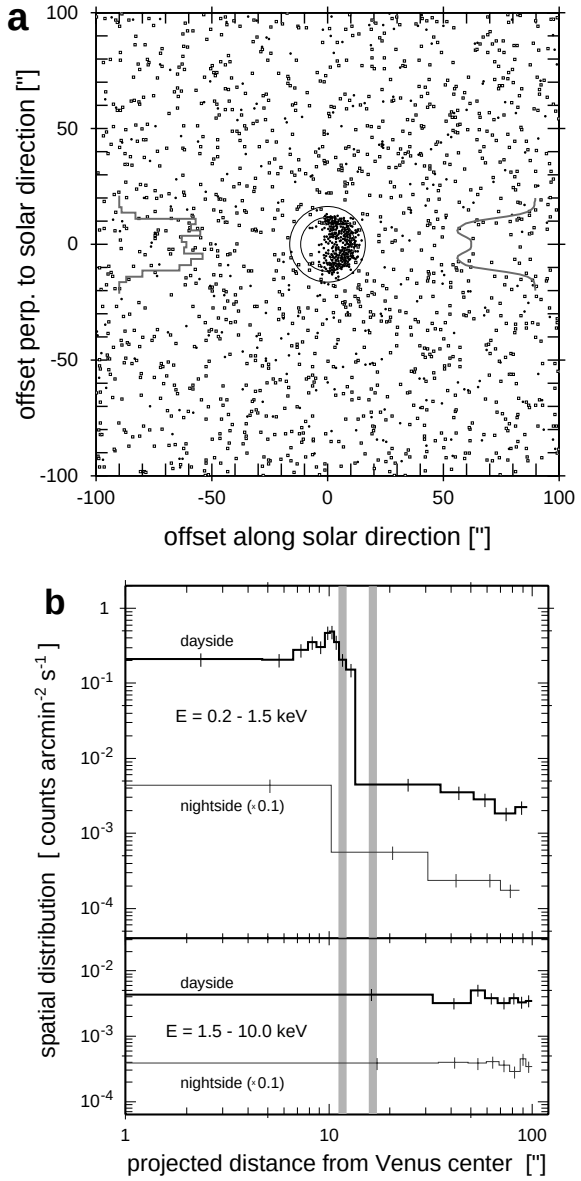

Fig. 2. Spatial distribution of photons around Venus in the ACIS–I observation. **a)** All photons in the energy range 0.2–10.0 keV; those with $E \leq 1.5$ keV are marked with black dots, while photons with $E > 1.5$ keV are plotted as open squares. In some cases the symbols have been slightly shifted (by typically less than $1''$) to minimize overlaps. Two circles are shown, the inner one, with $r = 11\farcs7$, indicating the geometric size of Venus, and the outer one, with $r = 16\farcs5$, enclosing practically all photons detected from Venus. The histogram to the left shows the distribution of photons with $E \leq 1.5$ keV from the outer circle, projected onto the y axis, with $2\farcs5$ resolution; the smoothed version to the right was used as a template for fitting the LETG spectrum. **b)** Spatial distribution of the photons in the soft ($E = 0.2-1.5$ keV) and hard ($E = 1.5-10.0$ keV) energy range, in terms of surface brightness along radial rings around Venus, separately for the "dayside" (offset along solar direction > 0) and the "nightside" (offset < 0). For better clarity the nightside histograms were shifted by one decade downward. The bin size was adaptively determined so that each bin contains at least 24 counts. Thick vertical lines mark the radii of $11\farcs7$ and $16\farcs5$ of the circles in **a)**.

separated by dispersion. To minimize the risk of telemetry overload, the area around the zero order image (contaminated by optical light) was not transmitted to Earth. The telescope was offset by $3\farcm25$ from its nominal aimpoint, to shift the most promising spectral region around the dispersed 0.53 keV O–K$_\alpha$ emission line well into the back–illuminated CCD S3 (Fig. 3). The combination of direct imaging and spectroscopy with the transmission grating made it possible to obtain complementary spatial and spectral information within the available total observing time of 6.5 hours.

At the time of the observation, Venus was moving across the sky with a proper motion of $2\farcm6$/hour. As the CCDs were read out every 3.2 s, there was no need for continuous tracking. The spacecraft was oriented such that Venus would move parallel to one side of the CCDs and perpendicular to the dispersion direction in the LETG observation. To keep Venus well inside the $8\farcm3$ field of view (FOV) of ACIS–S perpendicular to the dispersion direction, Chandra was repointed at the middle of the LETG/ACIS–S observation (Table 1). For ACIS–I with its larger $16\farcm9 \times 16\farcm9$ FOV, no repointing during the observation was necessary. As the photons were recorded time–tagged, an individual post–facto transformation into the rest frame of Venus is possible. This was done with the geocentric ephemeris of Venus as computed with the JPL ephemeris calculator[1]. Correction for the parallax of Chandra was done with the orbit ephemeris of the delivered data set. For the whole analysis we used events with Chandra standard grades and excluded bright pixels. The fact that all observations were performed with CCDs with intrinsic energy resolution made it possible to suppress the background with high efficiency.

3. Results

3.1. Morphology

In the X–ray image (Fig. 1) the crescent of Venus is clearly resolved and allows detailed comparisons with the optical appearance. An optical image (Fig. 8e), taken at the same phase angle, shows a sphere which is slightly more than half illuminated, closely resembling the geometric illumination, with the brightness maximum well inside the crescent. In the X–ray image the sphere appears to be less than half illuminated. The most striking difference, however, is the pronounced limb brightening, which is particularly obvious in the surface brightness profiles (Fig. 2b) and in the smoothed X–ray image (Fig. 8d). For a quantitative understanding of this brightening we performed a simulation of the appearance of Venus in soft X–rays, based on fluorescent scattering of solar X–ray radiation. This simulation will be described in Sect. 4.

The ACIS–I observation is well suited to investigate the X–ray environment of Venus outside the bright crescent, an area unaffected by optical loading. In Fig. 2 the

[1] Available at `http://ssd.jpl.nasa.gov/cgi-bin/eph`

distribution of photons within a $200'' \times 200''$ region around Venus is shown, together with the evolution of the surface brightness with increasing distance from Venus, for a soft ($E = 0.2$–1.5 keV) and a hard ($E = 1.5$–10.0 keV) band. In the soft band there is some indication that the surface brightness at $r = 16\farcs5$–$100''$ decreases with increasing distance from Venus, both at the day- and nightside. The fact that the corresponding distributions in the hard band are flat argues against the possibility that this drop is caused by inhomogeneities in the overall sensitivity. If the drop is not caused by other instrumental effects, e.g., the PSF of the telescope, then this could be evidence for an extended X–ray halo around Venus. This will be discussed further in Sect. 5.

3.2. Spectrum

The ACIS–I data clearly show that the X–ray spectrum of Venus is very soft: images accumulated from photons with energies $E > 1.5$ keV show no enhancement at the position of Venus (cf. Fig. 2b). We determine a $3\,\sigma$ upper limit of 2.5×10^{-4} counts/s to any flux from Venus in the 1.5–2.0 keV energy range. The corresponding value for $E = 2.0$–8.0 keV is 5.6×10^{-4} counts/s. Further spectral analysis of the ACIS–I data is complicated by the presence of optical loading[2].

Anticipating this possibility, and in order to fully utilize the spectroscopic capabilities of Chandra, we performed also spectroscopic observations with the LETG. Figure 3a shows what we expected to see in the dispersed first order spectra: images of the Venus crescent in the C–K_α, N–K_α and O–K_α emission lines (the energies were taken from Bearden 1967). Figure 3b shows the observed spectrum. The photons from both LETG observations were transformed into the rest frame of Venus and superimposed. Bright pixels and bright columns were excluded, and the intrinsic energy resolution of ACIS–S was used to suppress the background[3]. This spectrum, which is completely uncontaminated by optical light, clearly shows that most of the flux comes from O–K_α fluorescence. As this flux is monochromatic, images of the Venus crescent (illuminated from bottom) show up along the dispersion direction. The intensity profile along this direction is shown in Fig. 3c.

For the determination of the line energies we proceeded as follows: from the ACIS–I observation, we accumulated all photons with $E \leq 1.5$ keV within a circle of $r = 16\farcs5$ around Venus along the solar direction, to get the intensity profile perpendicular to the solar direction (Fig. 2a), i.e., along the dispersion axis in the LETG observation (Fig. 3). This profile, which shows a characteristic central dip due to the effect of limb brightening, was then smoothed with a cubic spline function and used as a template for the spectral fit. For each emission line, the position and the normalization of the template were determined as free parameters by χ^2 minimization. The dispersion was expressed in arcseconds, and the width of the template was reduced by 3% (to take the change of the apparent size into account; Table 1) and kept fixed. Errors were determined by increasing the minimum χ^2 by 1.0, with the normalization as free parameter. The results, converted into energies, are listed in Table 2.

The observed line energies are higher than the values of Bearden (1967), but in all cases the deviation is less than $1.5\,\sigma$. A better agreement, with deviations of less than $1.0\,\sigma$, is achieved with Aikin (1970), who quoted emission energies of 278.4, 392.9, and 526.0 eV for C, N, and O. Recent determinations of the dominant emission line of atomic oxygen (for the $1s2s^22p^5(^3P^O)$ configuration) yielded energies in the range 526.8 – 528.3 eV (McLaughlin & Kirby 1998, and references therein), which is in excellent agreement with the $527.2^{+1.3}_{-1.4}$ eV found in the LETG – S3 spectrum of Venus. If the oxygen atom is embedded in a molecule, this energy is slightly shifted: to 527.3 eV for CO_2 (Nordgren et al. 1997), 526.8 eV for O_2 (McLaughlin & Kirby 1998), and 525.0 – 526.0 eV for CO (Skytt et al. 1997). These shifts are too small to be discriminated with the currently available spectral resolution, which is mainly limited by the statistical uncertainty due to the low number of detected photons. The situation is similar for carbon and nitrogen, where the following values were recently found: 279.2 eV for CO (Skytt et al. 1997) and 393 – 394 eV for N_2 (Nordgren et al. 1997).

Emission line spectra of molecules composed of C, N, and O atoms are characterized by an additional fluorescence line, caused by the $1s \rightarrow \pi^\star$ transition following core excitation. In CO, this line is much more pronounced at the C than at the O fluorescence energy (e.g. Skytt et al. 1997, Figs. 5 and 6). The energies for the $1s \rightarrow \pi^\star$ transition are 287.4 eV for C in CO (Sodhi & Brion 1984), 290.7 eV for C in CO_2 (Hitchcock & Ishi 1987), 401.1 eV for N_2, 534.2 eV for O in CO (Sodhi & Brion 1984), and 535.4 eV for O in CO_2 (McLaren et al. 1987). We do not see such an additional line at N and O. The image of Venus at the energy of carbon, however, appears elongated along the dispersion direction (Fig. 3b), and the spectrum (Fig. 3c) does indicate the presence of a

[2] Although ACIS–I is equipped with an efficient filter for blocking optical light, the optical brightness of Venus (surface brightness: 1.5 mag per square arcsecond) is so extreme that a small fraction of optical photons succeed in penetrating the filter. These photons deposit charge in the CCD in addition to the X–ray photons, causing a systematic increase of the apparent energy. As a consequence, the spectrum of the photons within the optical extent of Venus ($r < 11\farcs7$) extends to higher energies than the one accumulated near the outer boundary ($11\farcs7 < r < 16\farcs5$), where only a fraction of photons (projected there by the PSF of the telescope) contributes to optical loading. Despite this contamination, both spectra indicate the presence of a bright emission line near 0.6 keV.

[3] This was done by selecting only events within $[E_{\min}, E_{\max}]$, with the energy boundaries depending on the displacement x from the zero order position:
$E_{\min} = 270\ \text{eV} + (E - 277\ \text{eV}) \cdot 0.8065$
$E_{\max} = 350\ \text{eV} + (E - 277\ \text{eV}) \cdot 1.0887$
$E = 1.239 \times 10^3\ \text{eV}/\lambda[\text{nm}]\,,\ \ \lambda/[\text{nm}] = 5.602 \times 10^{-3} \cdot |x['']|.$

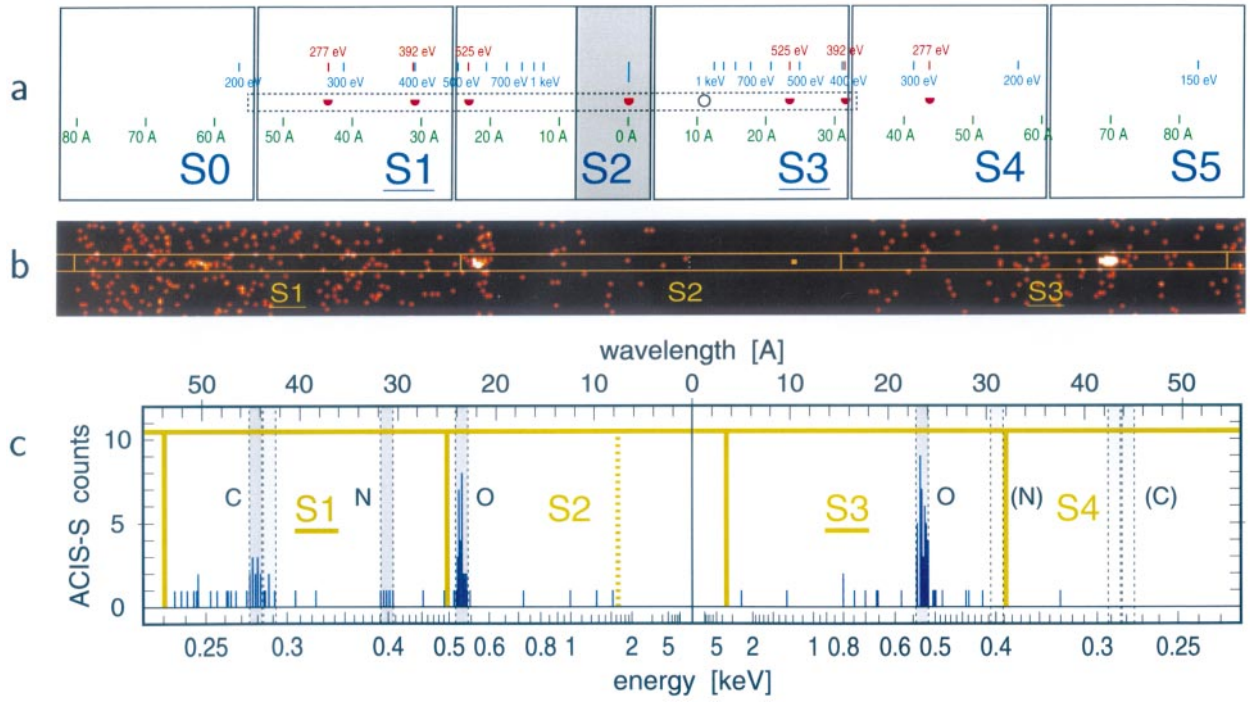

Fig. 3. a) Expected LETG spectrum of Venus on the ACIS–S array. S1 and S3 are back–illuminated CCDs with increased sensitivity at low energies (underlined), while the others are front–illuminated. The nominal aimpoint, in S3, is marked with a circle. The aimpoint was shifted by 3.25′ into S2, to get more of the fluorescent lines covered by back–illuminated CCDs. During the two parts of the observation, Venus was moving perpendicularly to the dispersion direction. In order to avoid saturation of telemetry, the shaded area around the zero order image in S2 was not transmitted. Energy and wavelength scales are given along the dispersion direction. Images of Venus are drawn at the position of the C, N, and O fluorescence lines, with the correct size and orientation. The dashed rectangle indicates the section of the observed spectrum shown below. **b)** Observed LETG spectrum of Venus, smoothed with a Gaussian function with $\sigma = 2\farcs0$. The two bright crescents symmetric to the center are images in the line of the O-K$_\alpha$ fluorescent emission, while the elongated enhancement at left is at the position of the C–K$_\alpha$ fluorescent emission line. The Sun is at bottom. Vertical lines mark the extent of the individual CCDs. The position of the zero order image (not transmitted) is indicated by a small square in S2. Contamination from higher orders is negligible. **c)** Spectral scan along the region outlined above. Scales are given in keV and Å. The observed C, N, and O fluorescent emission lines, at the energies listed in Table 2, are enclosed by dashed lines; the width of these intervals matches the size of the Venus crescent ($22\farcs8$). The thick lines mark the borders of the individual CCDs.

Table 2. Number of photons, derived fluxes, and line energies.

grating	line	CCD	type	eff area	photons	photon flux	energy flux	energy
LETG	C–K$_\alpha^\star$	S1	BI	14 cm^2	18 ± 8	1.1 ± 0.5	4.8 ± 2.1	$278.6\,^{+1.3}_{-1.1}$ eV
LETG	N–K$_\alpha$	S1	BI	5 cm^2	4 ± 2	0.6 ± 0.3	4.0 ± 2.0	$398.5\,^{+4.1}_{-5.9}$ eV
LETG	O–K$_\alpha$	S2	FI	7 cm^2	32 ± 7	3.8 ± 0.8	$32. \pm 7.0$	$527.7\,^{+4.6}_{-3.8}$ eV
LETG	O–K$_\alpha$	S3	BI	21 cm^2	50 ± 9	2.1 ± 0.4	17.2 ± 3.1	$527.2\,^{+1.3}_{-1.4}$ eV
none	(O–K$_\alpha$)	I 1, 3	FI	135 cm^2	274 ± 17	1.7 ± 0.1	14.4 ± 0.9	—

LETG: spectroscopy with grating, first order; none: direct imaging (not simultaneous with spectroscopy);
BI: back–illuminated, FI: front–illuminated; eff area: effective area used for the calculation;
photon flux in units of 10^{-4} ph cm^{-2} s^{-1}; energy flux in units of 10^{-14} erg cm^{-2} s^{-1}.
* There is some evidence for a secondary emission line at 288 ± 4 eV; the photons from this line were included in the flux determination for C–K$_\alpha$.

secondary emission line at 288 ± 4 eV, consistent with the energy of the C 1s $\rightarrow \pi^\star$ transition in CO_2 and CO.

Table 2 summarizes the number of detected photons in the individual lines together with the derived fluxes. The specified uncertainties are $1\,\sigma$ errors from photon statistics; they do not include uncertainties in the effective areas at $E < 0.6$ keV. This could be the reason for the $1.9\,\sigma$ deviation between the two O–K$_\alpha$ fluxes observed with S2 and S3, because both parts of the dispersed spectrum were recorded simultaneously. For C–K$_\alpha$ the

number of recorded photons is sufficient for detection, but not high enough for a reliable flux determination. For N–K$_\alpha$ a marginal detection is only possible because the few photons were recorded exactly at the expected position. The fact that no N–K$_\alpha$ photons are detected at the corresponding mirror site may be related to inhomogeneities in the ACIS–S low energy response, in particular close to the CCD borders. The last row in Table 2 contains the values for the direct imaging observation with ACIS–I. Despite the lower energy resolution and the problem with optical loading, it is very likely that most of the flux came from O–K$_\alpha$. The difference between this flux and the (non–simultaneously obtained) O–K$_\alpha$ fluxes from the LETG observations may be related to the X–ray variability of Venus (Sect. 3.3).

It is interesting to compare the total X–ray flux from Venus with the optical flux. The visual magnitude -4.4 mag corresponds to an optical flux of $f_{\rm opt} = 1.5 \times 10^{-3}$ erg cm^{-2} s^{-1}. Adopting a total X–ray flux of $f_{\rm x} = 3.0 \times 10^{-13}$ erg cm^{-2} s^{-1}, we get

$$f_{\rm x}/f_{\rm opt} = L_{\rm x}/L_{\rm opt} = 2 \times 10^{-10}.$$

Taking into account that the energy of a K$_\alpha$ photon exceeds that of an optical photon by two orders of magnitude, we find that on average there is only one X–ray photon among 5×10^{11} photons from Venus. This extremely small fraction of X–ray versus optical flux, combined with the soft X–ray spectrum and the proximity of Venus to the Sun, illustrates the challenge of observing Venus in X–rays. The X–ray flux is emitted in just three narrow emission lines. Outside these lines the $L_{\rm x}/L_{\rm opt}$ ratio is even orders of magnitude lower.

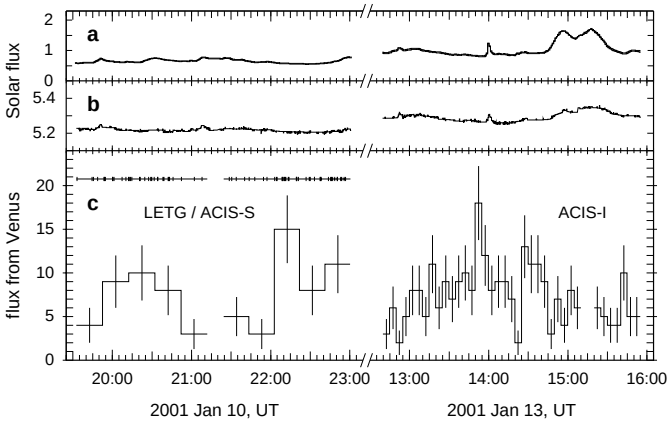

Fig. 4. Temporal behaviour of the soft X–ray flux from the Sun and Venus. **a)** 1–8 Å (1.55–12.4 keV) solar flux in 10^{-3} erg cm^{-2} s^{-1} at 1.0 AU, as measured with GOES–8 and GOES–10. **b)** 1–500 Å (0.025–12.4 keV) solar flux in 10^{10} photons cm^{-2} s^{-1} scaled to 1.0 AU, as measured with SOHO/SEM. The times in **a)** and **b)** were shifted by +240 s and +230 s for Jan. 10 and 13, to take the light travel time delay between Sun → Venus → Chandra and Sun → SOHO into account. **c)** X–ray flux from Venus as observed with Chandra LETG/ACIS–S and ACIS–I. The ACIS–S data are shown with 1189.6 s and 1151.2 s time resolution for the first and second part (to avoid partially exposed time bins). Only photons at the energy of the O–K$_\alpha$ emission line were taken from the first order LETG spectra; the background contribution is negligible (cf. Fig. 3). Individual photon arrival times are indicated at top together with the exposure duration. The ACIS-I count rates, shown with 300 s time resolution, were derived by extracting all photons below 1 keV from a circle of 16.″5 radius centered at Venus. The interruption at 15:15 UT is caused by Venus crossing the gap between CCD I1 and I3. With less than 0.1 background events per time bin the background is negligible.

3.3. Temporal variability

While there is practically no variation of the optical flux from Venus on time scales of hours and less, the X–ray flux shows indications for pronounced variability on time scales of minutes (Fig. 4c). A Kolmogorov–Smirnov test yields probabilities of only 1% for both the observation with LETG/ACIS–S and ACIS–I that the count rates are just statistical fluctuations around a constant value. As variability of the 1–10 keV solar flux by a factor of two on time scales of minutes is not uncommon (e.g. Fig. 4a), we expect the scattered solar X–rays from Venus to exhibit a similar variability. However, a direct comparison with the solar flux monitored simultaneously with GOES–8 and GOES–10 (Fig. 4a) and SOHO/SEM (Fig. 4b) does not show an obvious correlation. This may be related to the fact that solar X–rays are predominantly emitted from localized regions and that Venus saw a solar hemisphere which was rotated by 48.°0 (LETG/ACIS–S) and 46.°5 (ACIS–I) from the solar hemisphere facing Earth. Differences from the broad band solar X–ray flux (as measured with GOES/SOHO) may also arise due to the fact that the X–ray flux from Venus responds very sensitively to variability of the solar flux in a narrow spectral range just above the K edges. As will be shown in the next section, this is particularly the case for O–K$_\alpha$: while the C–K$_\alpha$ emission increases by only 7% if the coronal temperature rises by 8%, the O–K$_\alpha$ emission increases by 33%.

4. Modeling the X–ray appearance of Venus

Estimates on the X–ray luminosity of Venus due to scattering and fluorescence of solar x–rays have recently been made by Cravens & Maurellis (2001). We are, however, not aware of detailed predictions of how Venus would appear in X–rays. For comparison with the observed image we performed a numerical simulation of fluorescent scattering of solar X–rays in the atmosphere of Venus. We did not consider elastic scattering, as the corresponding luminosity is one order of magnitude below the fluorescence luminosity, according to Cravens & Maurellis (2001), and in agreement with the observed LETG spectrum (Fig. 3c).

The ingredients to the model are the composition and density structure of the Venus atmosphere, the photoabsorption cross sections and fluorescence efficiencies of the major atmospheric constituents, and the incident solar spectrum.

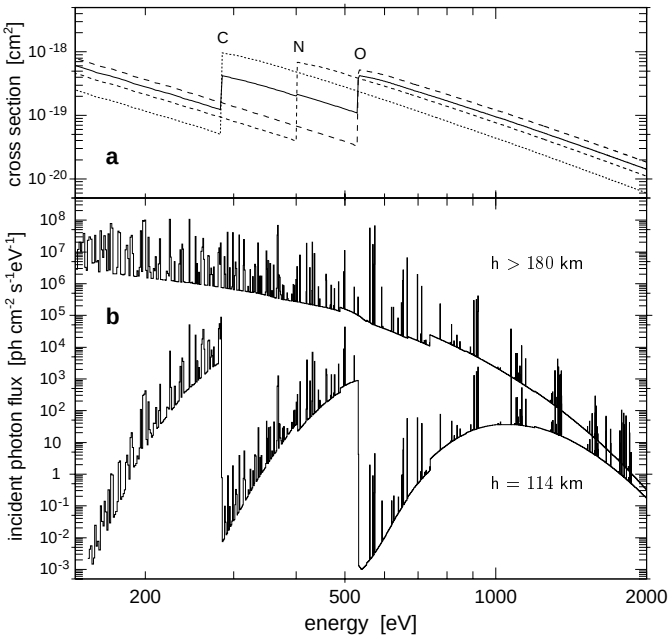

Fig. 5. a) Photoabsorption cross sections σ_C, σ_N, σ_O for C, N, and O (dashed lines), and σ_{CNO} for the chemical composition of the Venus atmosphere (solid line). **b)** Incident solar X–ray photon flux on top of the Venus atmosphere ($h > 180$ km) and at 114 km height (along subsolar direction; below). The spectrum is plotted in 1 eV bins. At 114 km, it is considerably attenuated just above the K_α absorption edges, recovering towards higher energies.

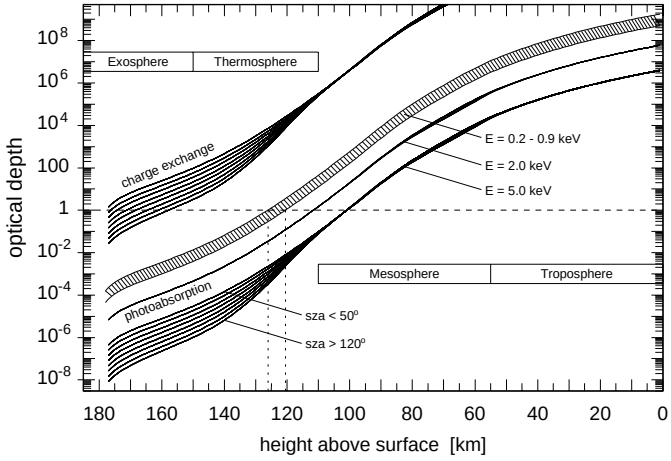

Fig. 6. Optical depth $\tau = \tau_C + \tau_N + \tau_O$ of the Venus model atmosphere with respect to charge exchange (above) and photoabsorption (below), as seen from outside. The upper/lower boundaries of the hatched area refer to energies just above/below the C and O edges (cf. Fig. 5a). For better clarity the dependence on the solar zenith angle (sza) is only shown for $E = 5.0$ keV; the curves for the other energies refer to sza $< 50°$. The dashed line, at $\tau = 1$, marks the transition between the transparent ($\tau < 1$) and opaque ($\tau > 1$) range. For a specific energy, the optical depth increases by at least 12 orders of magnitude between 180 km and the surface. For charge exchange interactions a constant cross section of 3×10^{-15} cm^2 was assumed.

4.1. Venus atmosphere

We adopted the Venus model atmosphere from Seiff (1983), where the density in the lower and middle atmosphere, i.e., between the surface and a height of 100 km, is tabulated in steps of 2 km for different latitudes, while for the upper atmosphere, between 100 km and 180 km, it is tabulated in steps of 4 km for two solar zenith angles sza (subsolar: sza $< 50°$ and antisolar: sza $> 120°$). For $50° \leq$ sza $\leq 120°$ we interpolated the density exponentially. In order to calculate the number density of C, N, and O atoms, we used the following values for the composition of the atmosphere: 65.2% oxygen, 32.6% carbon and 2.2% nitrogen. As the main constituents, C and O, are contained in CO_2, we assumed this composition to be homogeneous throughout the atmosphere.

4.2. Photoabsorption cross sections

The values for the photoabsorption cross sections were taken from Reilman & Manson (1979). We supplemented them with data from Chantler (1995) at energies close to the K edges. From these values and the C, N, and O contributions listed above, we computed the effective photoabsorption cross section of the Venus atmosphere (Fig. 5a). This, together with the atmospheric density structure, yielded the optical depth of the Venus atmosphere, as seen from outside (Fig. 6).

There is quite some discrepancy in the literature about the K–shell binding energies in C, N, and O atoms. These energies are affected by the outer electrons and thus depend on whether the element is in an atomic, molecular, or solid state. The values 283.8, 401.6, 532.0 eV for C, N, O, which Chantler (1995) computed for isolated atoms, are in good agreement with the values 283.84, 400, and 531.7 eV found by Henke et al. (1982) and used by, e.g., Morrison & McCammon (1983). However, Gould & Jung (1991) found significantly higher K–threshold energies for isolated C, N, and O atoms: 297.37 eV, 412.36 eV, and 546.02 eV. According to Snowden & Freyberg (1993), the values 400 eV and 532 eV of Henke et al. (1982) refer to molecular nitrogen and oxygen, while Ma et al. (1991) quote an ionization potential of 409.938 eV for N_2 (and 296.080 eV for C in CO). A compilation by Sevier (1979) lists calculated values of 296.94 eV for atomic carbon, 410.7 eV and 411.88 eV for atomic nitrogen, 411.2 eV for N_2, 545.37 eV for atomic oxygen, and 542.2 eV for O_2. An accurate treatment of the K–edge is further complicated by the presence of considerable fine–structure: detailed calculations of the inner–shell photoabsorption of oxygen by McLaughlin & Kirby (1998) show that already the atomic state contains an impressive amount of resonance structure around the K–edge.

In order to estimate the consequences of all these uncertainties, we ran our simulation also with the following, alternative set of K–edge energies: $E_{K_C} = 296.1$ eV, $E_{K_N} = 409.9$ eV, $E_{K_O} = 544.0$ eV. In both cases

we assumed that the energy will be emitted at 279.2, 393.5 and 527.3 eV, according to recent determinations and in agreement with the observed LETG spectrum (Sect. 3.2). We found no significant differences in the results (Table 3).

4.3. Solar radiation

The solar spectra for 2001 January 10 and 13 were derived from SOLAR 2000 (Tobiska et al. 2000)[4]. These spectra, best estimate daily average values, do not differ much between both dates. To improve the coverage towards energies $E > 100$ eV, we computed synthetic spectra with the model of Mewe et al. (1985) and aligned them with the SOLAR 2000 spectra in the range 50 – 500 eV, by adjusting the temperature and intensity. We derived a coronal temperature of 120 ± 10 eV. The spectrum, scaled to the heliocentric distance of Venus, is shown in Fig. 5b (upper curve), with a bin size of 1 eV, which we used in order to preserve the spectral details.

4.4. Model grid

The high dynamic range in the optical depth of the Venus atmosphere (Fig. 6) requires a model with high spatial resolution. For the simulation we choose a right–handed coordinate system (x, y, z) with the center of Venus at (0, 0, 0) and the Sun at $(0, 0, +\infty)$. We sample the irradiated part of the Venus atmosphere with a grid of volume elements of size $s_x = s_y = s_z \equiv s_\mathrm{g} = 1$ km.

Figure 6 shows that the atmosphere becomes optically thick for X–rays with $E < 5$ keV already at heights above 100 km. This means that solar X–rays do not reach the atmosphere below 100 km, where the density shows some latitudinal dependence. Above 100 km, however, the density of the model atmosphere depends only on the height and the solar zenith angle. This simplifies the calculation: instead of computing the solar irradiation of the volume elements $V(x_i, y_j, z_k)$, it is only necessary to do this for volume elements $V(r_{ij}, z_k)$, with $r_{ij} = (x_i^2 + y_j^2)^{1/2}$.

The whole information about the irradiation of the atmosphere can thus be computed and stored in volume elements $V_{ik} = V(r_i, z_{k_i})$, $i = 1...n$ and $k_i = 1...m_i$, with

$$n = \mathrm{int}[R_\mathrm{v}/s_\mathrm{g}] \quad \text{for} \quad r_i \le R_\mathrm{v} \quad \text{and}$$

$$m_i = \begin{cases} \mathrm{int}\left[\frac{1}{s_\mathrm{g}}\left(\left(R_\mathrm{v}^2 - r_i^2\right)^{1/2} - \left(r_\mathrm{v}^2 - r_i^2\right)^{1/2}\right)\right] & \text{for } r_i \le r_\mathrm{v} \\ \mathrm{int}\left[\frac{2}{s_\mathrm{g}}\left(R_\mathrm{v}^2 - r_i^2\right)^{1/2}\right] & \text{for } r_\mathrm{v} < r_i \le R_\mathrm{v}. \end{cases}$$

Here $r_\mathrm{v} = 6052.0$ km is the radius of Venus, $h_\mathrm{v} = 180$ km is the height of the model atmosphere, and $R_\mathrm{v} = r_\mathrm{v} + h_\mathrm{v}$.

With this grid the calculation is performed in two steps: in the first step the solar radiation absorbed in each volume element is calculated and stored. In the second step an image of Venus is accumulated for a particular phase angle by integrating the emission and subsequent absorption of the corresponding volume elements along the line of sight.

[4] Available at `http://SpaceWx.com/`

4.5. Simulation

The first step is performed by propagating the irradiation for each column i from the top of the atmosphere along the $-z$ direction, i.e., away from the Sun. For the center of the corresponding volume element V_{ik}, the mass densitity is calculated from the height above the surface and the solar zenith angle, by exponential interpolation of the nearest tabulated grid points in the Venus model atmosphere, and converted into a number density n_{ik} of the sum of C, N, and O atoms. From the column densities

$$\rho_{\ell,ik} = n_{ik} \cdot s_\mathrm{g} \cdot f_\ell, \quad \text{with } \ell = \mathrm{C, N, O}$$

and $f_\mathrm{C} = 0.326$, $f_\mathrm{N} = 0.022$, $f_\mathrm{O} = 0.652$, the optical depths $\tau_{\ell,ik}(E)$ are computed

$$\tau_{\ell,ik}(E) = \rho_{\ell,ik} \cdot \sigma_\ell(E)\ , \quad \tau_{ik}(E) = \sum_{\ell=1}^{3} \tau_{\ell,ik}(E)$$

to derive the attenuated solar spectrum $f_{ik}^\mathrm{sun}(E)$:

$$f_{ik}^\mathrm{sun}(E) = \begin{cases} f^\mathrm{Sun}(E) & \text{for} \quad k = m_i \\ f_{i,k+1}^\mathrm{sun}(E)\, \mathrm{e}^{-\tau_{i,k+1}(E)} & \text{for} \quad 0 < k < m_i \end{cases}$$

and the flux $f_{\ell,ik}^\mathrm{abs}(E)$ of absorbed photons which interact with K_ℓ electrons:

$$f_{\ell,ik}^\mathrm{abs}(E) = f_{ik}^\mathrm{sun}(E) \cdot \begin{cases} 0 & \text{for} \quad E < E_{\mathrm{K}_\ell} \\ 1 - \mathrm{e}^{-\tau_{\ell,ik}(E)} & \text{for} \quad E \ge E_{\mathrm{K}_\ell} \end{cases}$$

Here $f^\mathrm{Sun}(E)$ is the solar spectrum scaled to the heliocentric distance of Venus (Fig. 5b), and E_{K_ℓ} are the energies of the K absorption edges (Chantler 1995)[5]:

$$E_{\mathrm{K_C}} = 283.8 \text{ eV}, \quad E_{\mathrm{K_N}} = 401.6 \text{ eV}, \quad E_{\mathrm{K_O}} = 532.0 \text{ eV}.$$

Only a fraction of the photons which interact with K_ℓ electrons cause subsequent K_ℓ shell fluorescence emission:

$$f_{\ell,ik}^\mathrm{em}(E) = y_\ell \cdot f_{\ell,ik}^\mathrm{abs}(E)$$

with the fluorescent yields $y_\mathrm{C} = 0.0025$, $y_\mathrm{N} = 0.0055$ and $y_\mathrm{O} = 0.0085$ (Krause 1979). The resulting volume emissivity of fluorescence photons is shown in Fig. 7 for the subsolar atmospheric column and for a column at the terminator.

As the fluorescence photons are emitted at an energy E_ℓ which is below the corresponding K edge E_{K_ℓ} (see Sects. 3.2 and 4.2), they are not subject to subsequent K shell absorption by the same element. K shell absorption by lighter elements, however, is possible. All photons are subject to elastic scattering, but as this process is nearly isotropic, only weakly energy dependent and characterized by cross sections which are several orders of magnitude smaller than for photoabsorption, it should not much affect the distribution of photons along the line of sight. We treat the attenuation of the reemitted photon flux due to subsequent photoabsorption along the line of sight in a similar way as we did for the attenuation of the incident

[5] See Sect. 4.2 for an alternative set of E_{K_ℓ}.

Table 3. Numerical results of the simulation obtained for the geometry and mean solar activity during the LETG/ACIS–S observation, for which a coronal temperature $kT = 0.12 \pm 0.01$ keV was derived; the errors are the result of the uncertainty in this temperature. For the calculation of the energy flux and luminosity, fluorescence line energies of 279.2, 393.5, and 527.3 eV were used (Sect. 3.2).

line	photon flux	energy flux	luminosity
C–K$_\alpha$	2.30 ± 0.16	10.3 ± 0.7	15.6 ± 1.1 MW
N–K$_\alpha$	0.10 ± 0.02	0.6 ± 0.1	1.0 ± 0.2 MW
O–K$_\alpha$	3.10 ± 1.03	26.2 ± 8.7	39.6 ± 13.2 MW
with alternative K–edge energies (Sect. 4.2):			
C–K$_\alpha$	2.00 ± 0.14	9.0 ± 0.6	13.6 ± 0.9 MW
N–K$_\alpha$	0.09 ± 0.02	0.6 ± 0.1	0.9 ± 0.2 MW
O–K$_\alpha$	3.08 ± 1.03	26.0 ± 8.7	39.4 ± 13.1 MW

Photon flux in units of 10^{-4} ph cm^{-2} s^{-1}.
Energy flux in units of 10^{-14} erg cm^{-2} s^{-1}.

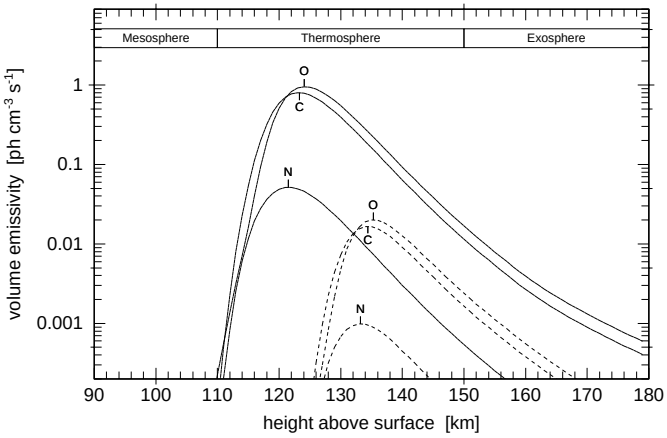

Fig. 7. Volume emissivities of C, N, and O K$_\alpha$ fluorescent photons at zenith angles of zero (subsolar, solid lines) and 90° (terminator, dashed lines) for the incident solar spectrum of Fig. 5b. The height of maximum emissivity rises with increasing solar zenith angles because of increased path length and absorption along oblique solar incidence angles. In all cases maximum emissivity occurs in the thermosphere, where the optical depth depends also on the solar zenith angle (Fig. 6).

solar flux, but this time only at the three discrete energies E_ℓ. By sampling the radiation in the volume elements along the line of sight, starting from the volume element which is farthest away from the observer, we can then accumulate images of Venus in the three energies E_ℓ in, e.g., orthographic projection, for any phase angle.

4.6. Results of the simulation

The simulated images of Venus at the K$_\alpha$ fluorescence energies C, N, and O are shown in Figs. 8a–c. They agree well with the observed X–ray image (Fig. 8d), while the optical image (Fig. 8e) is characterized by a different brightness distribution. In X–rays, Venus exhibits significant brightening at the sunward limb, accompanied by reduced brightness at the terminator, which causes it to appear less than half illuminated. This is a consequence of the fact that the volume emissivity extends into the tenuous, optically thin parts of the thermosphere and exosphere (Fig. 7). From there, the volume emissivities are accumulated along the line of sight without considerable absorption, so that the observed brightness is mainly determined by the extent of the atmospheric column along the line of sight. Detailed comparison of the images shows that the amount of limb brightening is different for the three energies. This can be understood in the following way.

If the incident solar spectrum consisted only of photons above the O–K$_\alpha$ edge, then the peak of volume emissivity would occur at the same height for all fluorescent lines, and this height would be determined by the spectral hardness of the incident solar flux. Differences in the height of the volume emissivity peak between C, N, and O occur due to the presence of photons with energies between the individual K$_\alpha$ edges. Photons with energies between N–K$_\alpha$ and O–K$_\alpha$, for example, influence the atmospheric height of maximum N–K$_\alpha$ emission, but do not affect the O–K$_\alpha$ peak. Due to the presence of such photons in the incident solar spectrum (Fig. 5b), which are affected by less photoabsorption (Fig. 5a) and penetrate deeper into the atmosphere, the nitrogen volume emissivity peak occurs at the lowest atmospheric heights (Fig. 7). In a similar way, the carbon emissivity peak lies just below that of oxygen.

Although the difference in the atmospheric heights of the individual peaks is only a few kilometers, this has consequences for the appearance of Venus in the individual fluorescence lines. At heights of ∼125 km, the density doubles every 3 km with decreasing height. The deeper in the atmosphere the emission occurs, the more absorbing layers are above. This effect is particularly important at the limb, where the column of absorbing material along the line of sight reaches a maximum, thus reducing the amount of limb brightening. Another factor which determines the amount of limb brightening is the photoabsorption cross section at the fluorescence energy. This energy is just below the corresponding K–edge (see Sects. 3.2 and 4.2). Figure 5a shows that for the chemical composition of the Venus atmosphere the photoabsorption cross section for nitrogen K$_\alpha$ fluorescence photons is about twice as large as that for carbon and oxygen K$_\alpha$ fluorescence photons, causing an additional attenuation of the limb brightness in the nitrogen image.

The simulations show that the limb brightening depends sensitively on the density and chemical composition of the Venus atmosphere. Thus, precise measurements of this brightening will provide direct information about the atmospheric stucture in the thermosphere and exosphere. With ACIS–I a brightening of 2.4 ± 0.6 was observed (Fig. 2b). From the computed images, smoothed with a Gaussian function with $\sigma = 1\farcs0$, we determine corresponding limb brightenings of 2.0 for C–K$_\alpha$, 1.7 for N–K$_\alpha$, and 2.2 for O–K$_\alpha$. The simulated images can also be used to derive the flux from the whole visible side

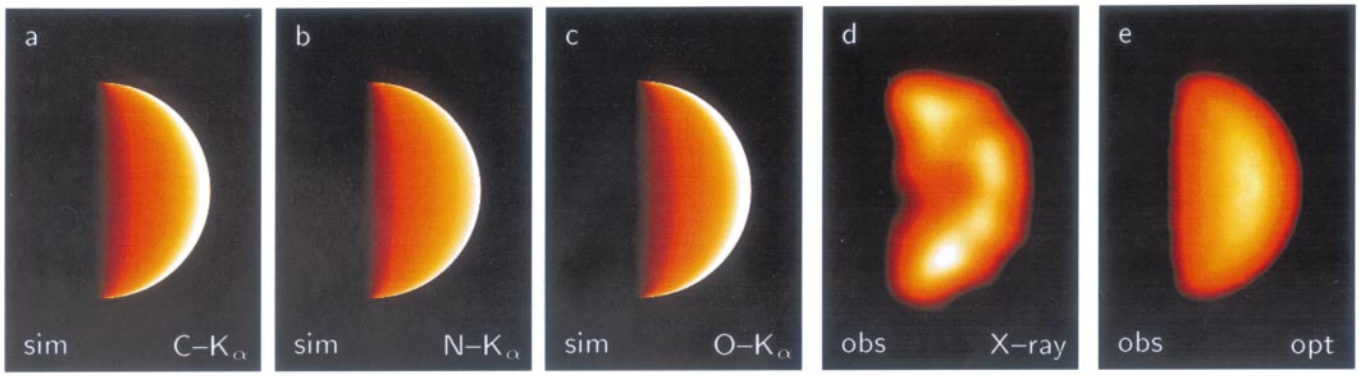

Fig. 8. a–c) Simulated X–ray images of Venus at C–K$_\alpha$, N–K$_\alpha$, and O–K$_\alpha$, for a phase angle $\varphi = 86.5°$. The X–ray flux is coded in a linear scale, extending from zero (black) to 1.2×10^6 ph cm^{-2} s^{-1} **a)**, 5.2×10^4 ph cm^{-2} s^{-1} **b)**, and 1.6×10^6 ph cm^{-2} s^{-1} **c)**, (white). All images show considerable limb brightening, especially at C–K$_\alpha$ and O–K$_\alpha$. **d)** Observed X–ray image: same as Fig. 1, but smoothed with a Gaussian filter with $\sigma = 1\farcs8$ and displayed in the same scale as the simulated images. This image is dominated by O–K$_\alpha$ fluorescence photons. **e)** Optical image of Venus, taken by one of the authors (KD) with a 4″ Newton reflector on 2001 Jan. 12.72 UT, 20 hours before the ACIS–I observation (cf. Table 1).

of Venus in the three energies. Table 3 shows that the derived flux values highly depend on the coronal temperature, in particular for O–K$_\alpha$. We derive from the simulation a total flux of $(3.6 \pm 0.9) \times 10^{-13}$ erg cm^{-2} s^{-1} for all three lines. The corresponding value obtained from the LETG/ACIS–S observation (Table 2) is $(4.1 \pm 0.8) \times 10^{-13}$ erg cm^{-2} s^{-1} or $(2.6 \pm 0.4) \times 10^{-13}$ erg cm^{-2} s^{-1}, depending on whether we take the O–K$_\alpha$ flux from the S2 or S3 CCD. Considering all the uncertainties, these values are in good agreement with each other.

In order to study the angular distribution of the scattered photons, we computed X–ray images of Venus for different phase angles φ (Fig. 9a). We scanned the full range of φ from 0° to 180° with a step size of 1°, and determined the corresponding X–ray intensities for the three emission lines by integrating the observed flux from the images. Figure 9b shows the result. It is evident that the intensity declines first very slowly, staying above half of its maximum value for $\varphi < 75°$. At $\varphi = 90°$, the intensity has dropped to ∼40%. This illustrates that the solar X–rays are preferentially scattered back towards the Sun. For larger phase angles the decline becomes faster. Between 170° and 175°, the intensity drops by a factor of two, and the X–ray crescent starts to evolve into a thin ring around the dark planet, which is seen fully developed at $\varphi = 180°$. This ring might be observable with sufficiently sensitive solar X–ray observatories immediately before and after the upcoming Venus transits on 8 June 2004 and 5/6 June 2012. However, such observations would be extremely challenging, as the intensity of the ring will be only 0.3% of the fully illuminated Venus.

By spherically integrating the X–ray intensity for the three energies (Fig. 9a) over phase angle, we determined the luminosities listed in Table 3. The total X–ray luminosity of Venus, 55 ± 14 MW, agrees well with the prediction of Cravens & Maurellis (2001), who estimated a luminosity of 35 MW with an uncertainty factor of about two.

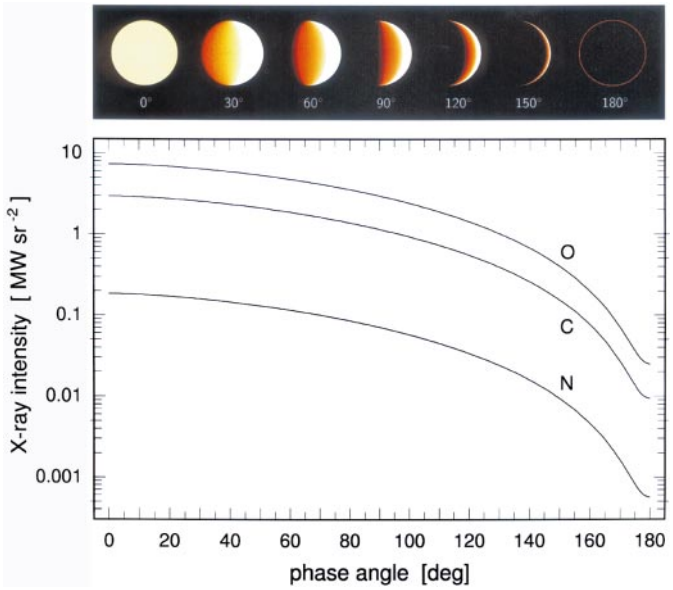

Fig. 9. X–ray intensity of Venus as a function of phase angle, in the fluorescence lines of C, N, and O. The images at top, all displayed in the same intensity coding, illustrate the appearence of Venus at O–K$_\alpha$ for selected phase angles.

5. Discussion

The Chandra data are fully consistent with fluorescent scattering of solar X–rays in the Venus atmosphere. This is an especially interesting result when compared with the X–ray emission of comets, where the dominant process for the X–ray emission is charge exchange between highly charged heavy ions in the solar wind and cometary neutrals. The LETG/ACIS–S spectrum (Fig. 3) definitively rules out that a similar process dominates the X–ray flux from the atmosphere of Venus at heights below ∼200 km.

The LETG/ACIS–S spectrum, however, does not exclude charge exchange interactions in the outer exosphere of Venus, as they would be too faint to be detected in the dispersed spectrum. A more sensitive method for

finding charge exchange signatures there is to look for enhancements of the surface brightness in the environment of Venus. In fact, the ACIS–I data do show indications for a decrease of the surface brightness with increasing distance from Venus from $20''$ to $100''$, in the energy range 0.2–1.5 keV (Fig. 2). We find the brightness at $r = 20''$ to exceed that at $r = 75''$ by $(2.7 \pm 1.0) \times 10^{-3}$ counts arcmin^{-2} s^{-1} on the dayside and by $(3.8 \pm 1.2) \times 10^{-3}$ counts arcmin^{-2} s^{-1} on the nightside. Both values are consistent with each other and yield a mean excess of $(3.3 \pm 0.8) \times 10^{-3}$ counts arcmin^{-2} s^{-1}.

Observations of comets in the ROSAT all–sky survey 1990–1991, also performed at solar maximum, show that the peak surface X–ray brightness which can be reached by charge exchange is $\sim 1.0 \times 10^{-13}$ erg cm^{-2} s^{-1} arcmin^{-2} at $r = 1$ AU for an average composition and density of the low–latitude solar wind (Dennerl et al. 1997); it scales with r^{-2}. This result is in good agreement with the theoretical estimate by Cravens (1997). Charge exchange produces a spectrum consisting of many narrow emission lines. The overall properties, however, can be approximated by 0.2 keV thermal bremsstrahlung emission (Wegmann et al. 1998). By applying this approximation to the ACIS–I observation, we obtain a maximum countrate due to charge exchange of $\sim 4.6 \times 10^{-3}$ counts arcmin^{-2} s^{-1} at $r = 0.72$ AU.

This maximum value is only slightly (by $48\% \pm 36\%$) larger than the excess observed at $r = 20''$, which implies that the exosphere should be almost collisionally thick 4300 km above the surface. At this height, however, both the hydrogen and the hot oxygen densities are $\sim 10^2$ cm^{-3} (Bertaux et al. 1982; Nagy & Cravens 1988) and thus orders of magnitude too low. Furthermore, the ACIS–I spectrum of all events within $16\farcs5$ and $100''$ radius around Venus (not affected by optical loading) shows no evidence for the spectral signatures observed in the ACIS–S spectrum of Comet C/1999 S4 (LINEAR), which were attributed to charge exchange interactions (Lisse et al. 2001). We conclude that the observed excess in the surface brightness is either spurious or produced by other effects.

At heights of 155–180 km, however, the exosphere of Venus does become collisionally thick due to the large cross section of charge transfer interactions (Fig. 6). This implies that if the flux of highly charged heavy solar wind ions reached these atmospheric layers, we would indeed observe the maximum flux estimated above. But even then not more than about 3 photons would have been detected due to charge exchange from the area of the crescent during the ACIS–I exposure. Taking the presence of an ionosphere into account, which shields the lower parts from the solar wind, then even this estimate appears to be too high. By integrating the X–ray production rate over altitude, starting at 500 km, the approximate location of the ionopause, where the density is dominated by the hot oxygen corona, Cravens (2000) estimated a luminosity of 10^5 W for the total X–ray luminosity of Venus due to charge exchange. With the 0.2 keV thermal bremsstrahlung approximation this would result in a total ACIS–I countrate of 1.6×10^{-5} counts s^{-1}, or only 0.2 counts accumulated during the whole observation. We conclude that the observation was not sensitive enough for detecting charge exchange signatures.

It is interesting to compare the X–ray properties of Venus with those of comets, where the X–ray emission is dominated by the charge exchange process, while fluorescent scattering of solar X–rays is negligible. This opposite behaviour is a direct consequence of the different cross sections of both processes and the way the gas is distributed.

The cross sections for charge exchange typically exceed 10^{-15} cm^2 and are thus at least three orders of magnitude greater than for fluorescent emission, which are 10^{-18} cm^2 and less in the energy range of interest (Fig. 5a). The gas in a cometary coma is distributed over a much larger volume and solid angle than in a planetary atmosphere. The particle density in a coma is too low to reach a column density for efficiently scattering solar X–rays, but high enough to provide a sufficient number of target electrons for charge exchange. The atmosphere of Venus, on the other hand, is so dense that it is optically thick even to fluorescent scattering (Fig. 6). As the solar wind ions become discharged already in the outermost parts, only a tiny fraction of the atmospheric electrons can participate in the charge exchange process. Additionally, the flux of incident solar wind ions is reduced by the presence of an ionosphere. Even in the absence of an ionosphere, the peak X–ray surface flux due to charge exchange would not exceed that of a comet (with a sufficiently dense coma), when exposed to the same solar wind conditions. But while the X–ray bright area is confined to less than one arcminute in diameter in the case of Venus, the bright part of the cometary X–ray emission can extend over tens of arcminutes, thus increasing the total amount of charge exchange induced X–ray photons by two orders of magnitude or more.

6. Summary and conclusions

The Chandra observation clearly shows that Venus is an X–ray source. From the X–ray spectrum and morphology we conclude that fluorescent scattering of solar X–rays is the main process for this radiation, which is dominated by the K_α emission lines from C, N, and O, plus some possible contribution from the C 1s $\rightarrow \pi^\star$ transition in CO_2 and CO. By modeling the X–ray appearance of Venus due to fluorescence, we have demonstrated that the amount of limb brightening depends sensitively on the properties of the Venus atmosphere at heights above 110 km. Thus, information about the chemical composition and density structure of the Venus thermosphere and exosphere can be obtained by measuring the X–ray brightness distribution across the planet at the individual K_α fluorescence lines. This opens the possibility of using X–ray observations for remotely monitoring the properties of regions in the Venus atmosphere which are difficult to investigate otherwise, and their response to solar activity.

Acknowledgements. SOLAR 2000 Research Grade v1.15 historical irradiances are provided courtesy of W. Kent Tobiska and SpaceWx.com. These historical irradiances have been developed with funding from the NASA UARS, TIMED, and SOHO missions. The SOHO CELIAS/SEM data were provided by the USC Space Sciences Center. SOHO is a joint European Space Agency, United States National Aeronautics and Space Administration mission.

References

Aikin, A. C. 1970, Nature, 227, 1334
Bearden, J. A. 1967, Rev. Mod. Phys., 39, 78
Bertaux, J. L., Lepine, V. M., Kurt, V. G., & Smirnov, A. S. 1982, Icarus, 52, 221
Chantler, C. T. 1995, J. Phys. Chem. Ref. Data, 24, 71
Cravens, T. E. 1997, Geoph. Res. Lett., 24, 105
Cravens, T. E. 2000, Adv. Space Res., 26, 1443
Cravens, T. E., & Maurellis, A. N. 2001, Geophys. Res. Lett., 28, 3043
Dennerl, K., Englhauser, J., & Trümper, J. 1997, Science, 277, 1625
Fink, H. H., Schmitt, J. H. M. M., & Harnden, Jr. F. R. 1988, A&A, 193, 345
Gould, R. J., & Jung, Y.-D. 1991, ApJ, 373, 271
Grader, R. J., Hill, R. W., & Seward, F. D. 1968, J. Geophys. Res., 73, 7149
Henke, B. L., Lee, P., Tanaka, T. J., Shimabukuro, R. L., & Fujikawa, B. K. 1982, Atom. Data Nucl. Data Tables, 27, 1
Hitchcock, A. P., & Ishi, I. 1987, J. Electron Spectrosc. Relat. Phenom., 42, 11
Krause, M. O. 1979, J. Phys. Chem. Ref. Data, 8, 307
Lisse, C. M., Christian, D. J., Dennerl, K., et al. 2001, Science, 292, 1343
Lisse, C. M., Dennerl, K., Englhauser, J., et al. 1996, Science, 274, 205
Ma, Y., Chen, C. T., Meigs, G., Randall, K., & Sette, F. 1991, Phys. Rev. A, 44, 1848
McLaren, R., Clark, S. A. C., Ishii, I., & Hitchcock, A. P. 1987, Phys. Rev. A, 36, 1683
McLaughlin, B. M., & Kirby, K. P. 1998, J. Phys. B: At. Mol. Phys., 31, 4991
Mewe, R., Gronenschild, E. H. B. M., & van den Oord, G. H. J. 1985, A&AS, 62, 197
Morrison, R., & McCammon, D. 1983, ApJ, 270, 119
Mumma, M. J., Krasnopolsky, V. A., & Abbott, M. J. 1997, ApJ, 491, L125
Nagy, A. F., & Cravens, T. E. 1988, Geophys. Res. Lett., 15, 433
Nordgren, J., Glans, P., Gunnelin, K., et al. 1997, Appl. Phys. A, 65, 97
Reilman, R. F., & Manson, S. T. 1979, ApJS, 74, 815
Russell, C. T., Saunders, M. A., & Luhmann, J. G. 1985, Adv. Space Res., 5, 177
Seiff, A. 1983, in Venus, ed. D. M., Hunten, L., Colin, T. M., Donahue, & V. I., Moroz (The University of Arizona Press, Tucson, Arizona), 1045
Sevier, K. D. 1979, Atom. Data Nucl. Data Tables, 24, 323
Skytt, P., Glans, P., Gunnelin, K., Guo, J., & Nordgren, J. 1997, Phys. Rev. A, 55, 146
Snowden, S. L., & Freyberg, M. J. 1993, ApJ, 404, 403
Sodhi, R. N. S., & Brion, C. E. 1984, J. Electron Spectrosc. Relat. Phenom., 34, 363
Tobiska, W. K., Woods, T., Eparvier, F., et al. 2000, J. Atm. Solar Terr. Phys., 62, 1233
Wegmann, R., Schmidt, H. U., Lisse, C. M., Dennerl, K., & Englhauser, J. 1998, Planet. Space Sci., 46.5, 603